Article | Open Access

Energy Materials

Ghani et al. Energy Mater. 2026, 6, 600107 DOI:10.20517/energymater.2026.89

First-principles investigation of topological vanadium chalcogenide monolayers for synergistic sodium storage and sulfur conversion

Awais Ghani[1,*], Shehzad Ahmed[2,*], Muhammad Bilal[3], Adil Murtaza[4], Hongliang Du[1], Imran Muhammad[5,*]

Keywords:
Density functional theory, alkali ions, diffusion barrier, sodium-sulfur battery, gibbs energy, charge density

Citation: Ghani, A.; Ahmed, S.; Bilal, M.; Murtaza, A.; Du, H.; Muhammad, I. First-principles investigation of topological vanadium chalcogenide monolayers for synergistic sodium storage and sulfur conversion. *Energy Mater.* **2026**, *6*, 600107. https://dx.doi.org/10.20517/energymater.2026.89

Received: 25 Apr 2026
First Decision: 29 May 2026
Revised: 3 Jul 2026
Accepted: 27 Jul 2026
Published: 25 Aug 2026

Academic Editor:
Yuping Wu
Copy Editor:
Ping Zhang
Production Editor:
Ping Zhang

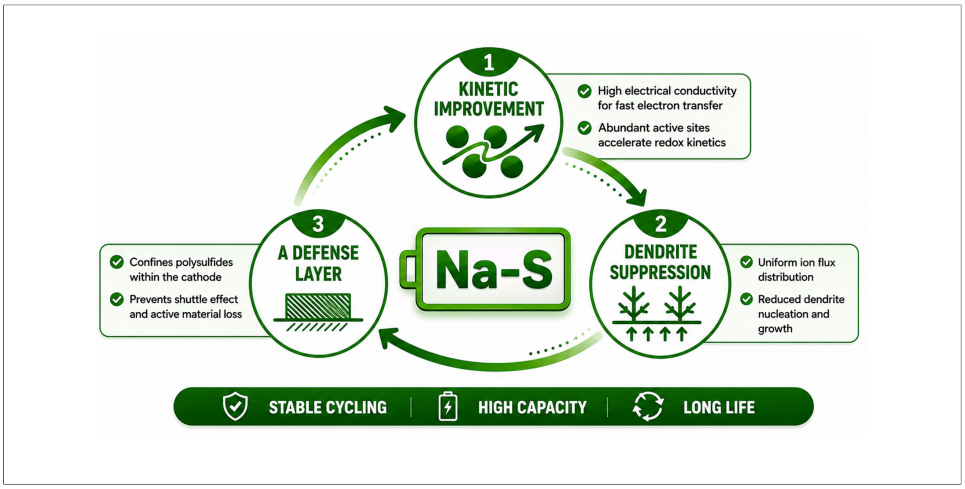

Abstract

An atomic-level understanding of anion and cation intercalation is essential for advancing alkali-metal-ion electrodes and anchoring metal polysulfides. Sodium batteries present a more sustainable alternative to lithium-based systems. Developing electrode materials that support both sodium-ion storage and sodium-polysulfide conversion, each in its own cell configuration, is therefore of growing interest. In this study, two-dimensional quaternary vanadium-based chalcogenides (V_2WS_4, V_2WSe_4, V_2MoS_4, and V_2MoSe_4) are computationally investigated. They exhibit indistinguishable bonding environments, topological band gaps, and versatility across two distinct cell configurations: sodium-ion storage and polysulfide anchoring. The distinctive topological electronic properties of these monolayers enhance Na^+/K^+ adsorption and facilitate high charge flux, indicating strong chemisorption while maintaining conductivity. These materials exhibit rapid ion transport,

[1]Multifunctional Electronic Ceramics Laboratory, College of Engineering, Xi'an International University, Xi'an 710077, Shaanxi, China.
[2]China-UK Low Carbon College, Shanghai Jiao Tong University, Shanghai 201306, China.
[3]Department of Mathematics and Industrial Engineering, Polytechnique Montréal, Montréal H3T 1J4, Canada.
[4]Guangdong Provincial Key Laboratory of Sensing Physics and System Integration Applications, School of Physics and Optoelectronic Engineering, Guangdong University of Technology, Guangzhou 510006, Guangdong, China.
[5]School of Energy, National Industry-Education Platform of Energy Storage, Tianjin University, Tianjin 300350, China.

*Correspondence to: Dr. Awais Ghani, Multifunctional Electronic Ceramics Laboratory, College of Engineering, Xi'an International University, Xi'an 710077, Shaanxi, China. E-mail: awaisghani@xaiu.edu.cn; Dr. Shehzad Ahmed, China-UK Low Carbon College, Shanghai Jiao Tong University, Shanghai 201306, China. E-mail: shehzadahmed@sjtu.edu.cn; Dr. Imran Muhammad, School of Energy, National Industry-Education Platform of Energy Storage, Tianjin University, Tianjin 300350, China. E-mail: imrankhan25@tju.edu.cn

as evidenced by low diffusion barriers of 0.22 eV and 0.16 eV for Na^+ and K^+ ions, respectively, and deliver higher capacities of up to 1,151 mAh g^{-1} for Na^+ and 821.9 mAh g^{-1} for K^+ compared to conventional graphitic electrodes, along with a low open-circuit voltage of approximately 0.21 V. Additionally, these materials suppress polysulfide shuttling via energetic anchoring and accelerate the reduction reactions, particularly for long-chain sodium polysulfides. Sulfur reduction reactions and kinetic calculations for sodium-sulfur clusters indicate that V_2MoSe_4 exhibits the lowest rate-limiting free-energy change, while V_2MoS_4, V_2WS_4, and V_2WSe_4 demonstrate moderate kinetics and redox stability. These vanadium-based topological chalcogenides are thus promising anode materials for sodium-ion storage and as anchoring platforms for sodium-sulfur battery cathodes.

INTRODUCTION

Though lithium-ion batteries (LIBs) have revolutionized large-scale energy storage, they still face constraints, namely escalating costs and limited lithium availability. To address these constraints and problems, sodium-ion batteries (NIBs) offer a promising alternative because sodium is abundant in the Earth's crust (on the order of ~2-3 wt%, versus ~0.002 wt% for lithium), while retaining electrochemical behavior similar to that of LIBs[1-3]. Recent progress in layered oxides, polyanionic compounds, and Prussian blue cathodes, along with a hard carbon anode, has brought NIBs closer to commercialization[4,5]. However, the larger ionic radius of the Na^+ ion results in relatively slow kinetics and reduced structural stability[6,7]. Likewise, potassium-ion batteries (KIBs) benefit from even greater abundance and a lower redox potential [-2.93 V *vs.* Standard Hydrogen Electrode (SHE)] but suffer from more severe kinetic barriers due to the even larger size of K^+[8-10]. Developing electrode materials for Na^+/K^+ storage that match the electrochemical performance of conventional lithium-ion batteries is therefore a critical objective. Beyond intercalation chemistry, sulfur-anchoring cathodes have garnered considerable interest due to their high theoretical energy density (1,274 Wh kg^{-1} for Na-S batteries)[11,12]. However, sulfur cathodes are still limited by three critical bottlenecks: (i) low electronic and ionic conductivity; (ii) volumetric expansion during cycling, causing structural pulverization; and (iii) the dissolution of long-chain metal polysulfides in liquid electrolytes, causing the shuttle effect that leads to anode corrosion and active sulfur loss[13,14]. Previously reported hosts, including MXenes[15], tellurides[16], transition-metal oxides, carbides[17], sulfides[18], and nitrides[19], have shown significant potential for anchoring sulfur and suppressing its shuttling. Thus, the development of high-performance Na^+ batteries is essential to meet the increasing demand for practical, high-energy-density batteries. Vanadium chalcogenides are considered competitive materials for energy storage applications due to their conductive nature and layered crystal structures, which facilitate rapid kinetics and ion storage capabilities[20-23]. In particular, vanadium chalcogenides, such as VSe_2[24], VS_2[25], VTe_2[26], V_5S_8-graphite hybrid nanosheet[27], and V_2O_5@MoS_2 nanocomposite[28], have been investigated for diverse electrochemical energy-storage applications. A new family of vanadium-based materials has also emerged, featuring a topological band structure, higher electrical conductivity, and favorable physicochemical characteristics. This group includes compounds such as KV_3Sb_5[29], CsV_3Sb_5[30], RbV_3Sb_5[31], YV_6Sn_6[32], GdV_6Sn_6[32], and ScV_6Sn_6[33], featuring nontrivial topological electronic properties with stable Dirac states that make them suitable for ion storage and sulfur anchoring. Materials with pronounced spin-orbital coupling and intrinsic polarities are competitive for Na-S batteries, owing to their anchoring capability for sulfur capture[34]. These properties open new avenues for quantum materials in electrochemical energy storage technologies. Importantly, a new family of vanadium-based topological chalcogenides with the unique stoichiometry V_2AB_4 (A = Mo, W; B = S, Se) has emerged, predicted to be quantum anomalous Hall insulators arising from the interplay of intrinsic ferromagnetism and strong spin-orbit coupling in the V and transition-metal d-orbitals[35]. These distinctive topological properties open new opportunities for the design of high-performance electrode and sulfur-host materials. While freestanding V_2AB_4 monolayers have not yet been synthesized directly, several experimental precedents support their feasibility. Ternary chalcogenides with the same A_2BX_4 stoichiometry have been realized and exfoliated to the single-layer limit; the Cu_2MX_4 family (M = Mo, W; X = S, Se) has been prepared

by solvothermal routes[36,37], and ultrathin two-dimensional ternary chalcogenide nanosheets such as Cu_2MoS_4 have been obtained by high-yield exfoliation[38]. The broader family of layered ternary transition-metal chalcogenides ($MM'X_4$) likewise has established synthetic routes; single-crystal $TaIrTe_4$, a topological ternary chalcogenide, has been grown from the melt and exfoliated to nanolayers[39]. Moreover, the constituent vanadium-based 2D chalcogenides have been grown as high-quality monolayers, including VSe_2 by molecular-beam epitaxy[40] and monolayer 1T-VS_2 [41]. The experimental accessibility of A_2BX_4 ternary chalcogenides, of the $MM'X_4$ structural family, and of V-based 2D chalcogenide monolayers together provides a credible basis for synthesizing the proposed V_2AB_4 monolayers via bottom-up growth (MBE/CVD) or exfoliation of a layered bulk parent, which we identify as the necessary next step toward practical electrodes.

In this work, we explored four topological vanadium-based chalcogenides, namely V_2WS_4, V_2WSe_4, V_2MoS_4, and V_2MoSe_4, and their versatility across two distinct cell configurations: as anodes for NIBs and KIBs, and as sulfur hosts for Na-S cathodes. Here, K-ion storage is considered only as a comparative alkali-ion anode assessment to examine the structural tolerance and ion-storage versatility of V_2AB_4 monolayers toward larger alkali ions, whereas the sulfur-host and catalytic conversion analysis is restricted to Na-S battery chemistry. Our combined first-principles and ab initio molecular dynamics simulations reveal the thermal stability of the host, its interaction with Na ions and sulfur species, Na^+ migration kinetics, and its catalytic activity toward polysulfide conversion, highlighting the practical relevance of these materials for future energy applications.

COMPUTATIONAL METHODS

All density functional theory (DFT) calculations were performed using the Vienna Ab initio Simulation Package (VASP) with the projector-augmented-wave (PAW) method to describe electron-ion interactions[42,43]. The generalized gradient approximation (GGA) with the Perdew-Becke-Johnson damping was applied with the DFT-D3 dispersion correction throughout[44]. To properly describe the van der Waals interactions within the interlayer of these layered V_2AB_4 structures, Becke-Johnson damping is used with the DFT-D3 dispersion correction throughout[45,46]. Given the presence of localized *d*-electrons on vanadium and other transition-metal (A = Mo, W) atoms, we have used the GGA+U[47] approach with Hubbard U corrections: U = 3.0 eV for V 3d states, 2.0 eV for Mo 4d states, and 1.0 eV for W 5d states[35]. A plane-wave energy cutoff of 520 eV was used for all structural relaxations and electronic-structure calculations. The two-dimensional monolayer structures are simulated using periodic slabs separated by a vacuum spacing of 25 Å along the *z*-direction to avoid spurious interactions between periodic images. The Brillouin zone sampling was carried out using Γ-centered Monkhorst-Pack k-point grids: a dense 12 × 12 × 1 mesh is employed for the primitive unit cells during structural optimization and self-consistent electronic structure calculations, and a 8 × 8 × 1 mesh for larger supercells. Electronic self-consistency was achieved when the total-energy difference between consecutive iterations fell below 1×10^{-5} eV, and the ionic relaxations were converged until the Hellmann-Feynman forces on all atoms were below 0.02 eV $Å^{-1}$. Phonon dispersion spectra were obtained using the finite-displacement method implemented in the PHONOPY package, interfaced with VASP[48,49]. To assess thermal stability at finite temperatures, *ab initio* molecular dynamics (AIMD) simulations were performed in the canonical (NVT) ensemble using the Nose-Hoover thermostat[50,51]. Diffusion barriers and migration pathways of ions on the V_2AB_4 surfaces were calculated using the climbing-image nudged elastic band (CI-NEB) method[52]. To evaluate the V_2AB_4 materials as sulfur hosts for Na-S battery applications, the adsorption energies of relevant sulfur species were calculated, including elemental sulfur (S_8), long-chain sodium polysulfides (Na_2S_8, Na_2S_6, and Na_2S_4), and short-chain species (Na_2S_2 and Na_2S). To evaluate the thermodynamic feasibility of the sulfur reduction reaction (SRR), the Gibbs free-energy change for each elementary step was calculated under standard conditions. The calculations were performed at T = 298.15 K. The Gibbs free-energy change was evaluated using:

$$\Delta G = \Delta E_{DFT} + \Delta E_{ZPE} - T\Delta S \quad (1)$$

where ΔE_{DFT} is the DFT reaction energy, ΔE_{ZPE} is the zero-point-energy correction, ΔS is the entropy change, and T is the temperature[53].

RESULTS AND DISCUSSION

Geometric and electronic characteristics

The overall concept of employing topological quantum materials for energy storage applications is illustrated in Figure 1A. This schematic highlights their potential across two distinct applications: metal-ion battery anodes and Na-S hosts. The four monolayers V_2MoS_4, V_2MoSe_4, V_2WS_4, and V_2WSe_4 obey the molecular formula V_2AB_4 and the space group P-42m. Each unit cell consists of three layers: a central V_2A layer sandwiched between two chalcogen layers. Four chalcogen atoms coordinate each V and A atom to form tetrahedral units, as shown in Figure 1A. The optimized lattice constants for V_2MoS_4, V_2MoSe_4, V_2WS_4, and V_2WSe_4 are 5.72, 5.83, 5.74, and 5.82 Å, respectively, increasing from S to Se due to the larger atomic radius of Se. However, the W and Mo atoms contribute only a minor change due to their nearly identical atomic radii. In addition to structural characterization, the thermal and dynamical stability of V_2MoS_4, V_2MoSe_4, V_2WS_4, and V_2WSe_4 monolayers are investigated. Thermal stability was verified using AIMD simulations at 300 K and 500 K for 5 ps, as shown in Figure 1B and Supplementary Figures 1-3 of the Supplementary Materials. These simulations demonstrate that all monolayers maintain structural integrity with no bond breaking or phase transitions, confirming excellent thermal stability. Phonon dispersion calculations along the high-symmetry path reveal no imaginary frequencies across the entire Brillouin zone for all four materials, confirming their dynamical stability as depicted in Figure 1C. Overall, these materials possess dynamic, structural, and thermal stability, indicating potential for further electronic and battery applications.

In addition, the electronic band gaps are investigated by calculating spin-polarized band structures with spin-orbit coupling (SOC) along high-symmetry paths in the Brillouin zone to examine the SOC-induced evolution of the electronic states [Figure 1D]. For V_2MoS_4, V_2MoSe_4, V_2WS_4, and V_2WSe_4, the band structures without SOC exhibit several band crossings near the Fermi level, mainly associated with spin-polarized V_d states hybridized with A-site (A = Mo, W) d states, where no obvious band gap is observed (see Supplementary Figure 4 in Supplementary Materials). After the inclusion of SOC, these degeneracies are lifted and finite gaps open at the high-symmetry points in Figure 1D. This gap opening originates from the SOC-induced splitting of the spin-polarized quadratic band touching of the degenerate V d_{xz}/d_{yz} orbitals, together with the band inversion between these Vd states and the A-site d states, producing a topologically nontrivial insulating electronic structure. These band-structure features spin-polarized d-orbital band crossings, band inversion between the V d_{xz}/d_{yz} and A-site (Mo/W) d orbitals, and the SOC-driven gap opening are characteristic of the pristine V_2AB_4 monolayers, whose nontrivial topological nature has been established in a prior study[35]. The high stability and favorable electronic structure position the V_2AB_4 vanadium chalcogenides as compelling candidates for ion-battery applications.

Na^+/K^+ ions anodic application

The suitability of V_2AB_4 surfaces as high-rate anodes was evaluated by systematically identifying three energetically favorable adsorption sites (a, b, and c) and examining their interactions with Na^+ and K^+ ions. The adsorption sites are defined as follows: site-a is located directly above the chalcogen B atom (S or Se), site-b is positioned above the A atom (Mo or W) coordinated by neighboring chalcogen atoms, and site-c is situated directly atop a V atom. Na^+ and K^+ atoms were initially placed approximately 2.5 Å above the monolayer plane, and the entire system was fully relaxed to determine equilibrium geometries and adsorption energies as depicted in Figure 2A. Adsorption energies for Na^+ and K^+ ions on all four V_2AB_4-type materials were calculated including van der Waals (vdW) corrections, with the corresponding values presented in Figure 2B. Site-a was identified as the most stable adsorption site for both Na^+ and K^+ ions, with

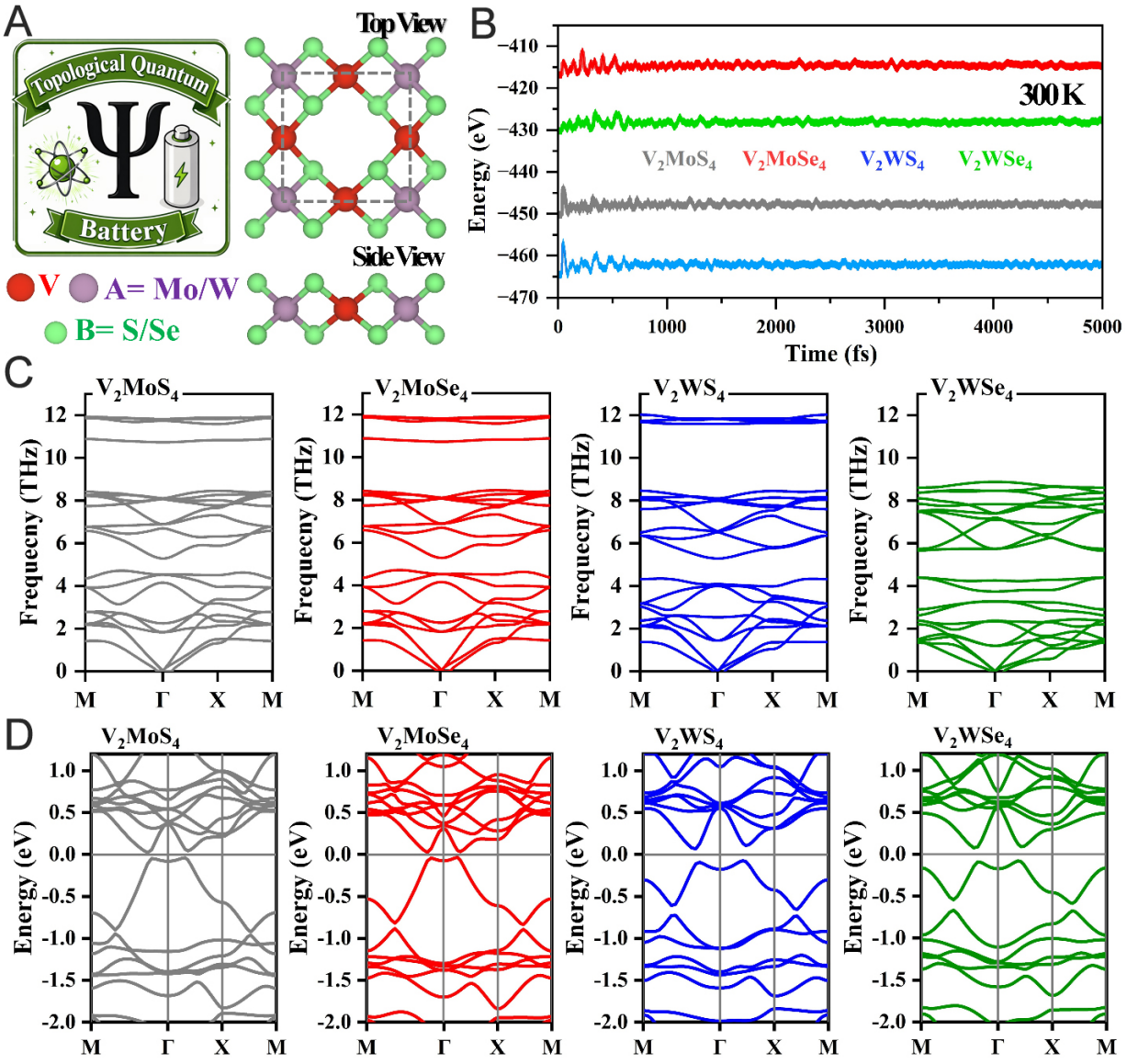

Figure 1. Geometric and electronic properties of vanadium-based topological chalcogenides: (A) schematic illustration of topological quantum materials for battery applications, along with the top and side views of four optimized crystal structures with stoichiometric formulas of V_2AB_4; (B) Potential energy fluctuations during AIMD simulations at 300 K for 5 ps; (C) phonon dispersion curve describing dynamic stabilities; and (D) topological band structures of V_2MoS_4, V_2MoSe_4, V_2WS_4, and V_2WSe_4 monolayers using the SOC method. SOC: Spin-orbit coupling; AIMD: *ab initio* molecular dynamics.

adsorption energies ranging from -1.19 eV to -1.36 eV for Na^+ and -1.36 eV to -1.83 eV for K^+. Site-b was the second most stable site, exhibiting adsorption energies approximately 0.25-0.35 eV higher (less negative) than those of site-a, while site-c was the least favorable. The preference for site-a arises from its optimal coordination environment for the ions. At this site, both Na^+ and K^+ lie equidistant from six neighboring chalcogen atoms (three from the top layer and three from the bottom layer). This configuration provides the maximum possible electrostatic stabilization and charge transfer from the alkali metal to the substrate.

Improved ion cycling stability is aided by rapid ion flux, which helps limit structural degradation during charge and discharge. The diffusion kinetics of Na^+ and K^+ ions on the V_2AB_4 (A = Mo/W, B = S/Se) monolayers are systematically studied by the CI-NEB method. Figure 2A illustrates that the most favorable diffusion pathway involves in-plane migration between two neighboring sites a through the transition site.

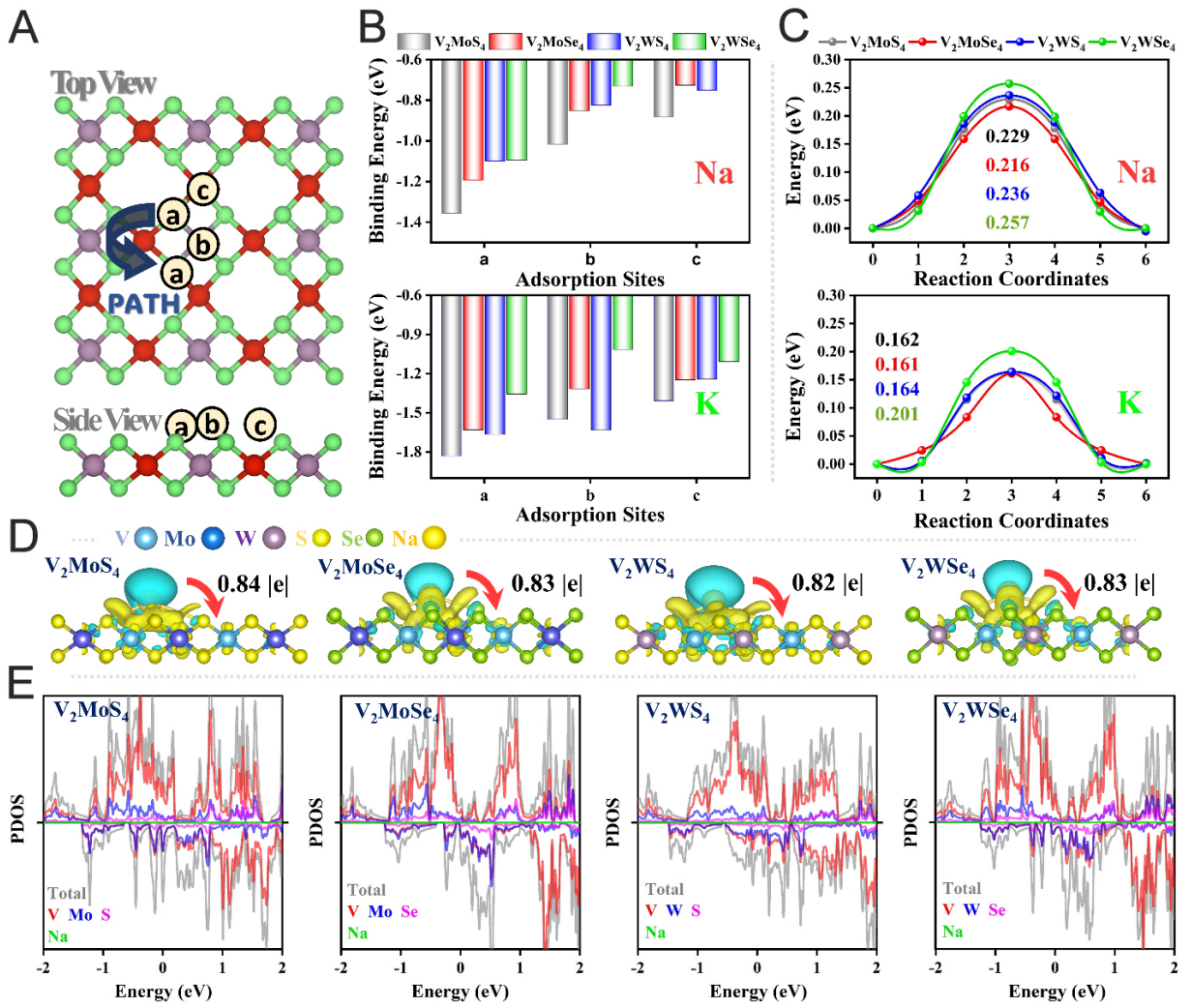

Figure 2. Sodium and potassium adsorption energetics, Diffusion Barrier, charge-transfer behavior, and the corresponding densities of states of V_2AB_4: (A) Geometric illustration of active energetic sites (a, b, and c), and (B) adsorption energies for Na^+ and K^+ ions on all four V_2AB_4-type monolayers; (C) CI-NEB energy profiles for V_2MoS_4, V_2MoSe_4, V_2WS_4, and V_2WSe_4; Visualization of (D) charge-density difference with corresponding Bader charge transfer from Na^+ ions to V_2AB_4 surfaces (Yellow and cyan represent electron gain and electron loss, respectively, with the isosurface value of 0.002 e $Å^{-3}$); (E) Na^+ induced projected density of states (PDOS) on V_2AB_4 monolayers. CI-NEB: Climbing-image nudged elastic band.

Figure 2C presents the corresponding CI-NEB energy profiles for Na^+ and K^+ diffusion across V_2MoS_4, V_2MoSe_4, V_2WS_4, and V_2WSe_4, respectively. For Na^+ ions, the migration barrier is found to be 0.229, 0.216, 0.236, and 0.257 eV for V_2MoS_4, V_2MoSe_4, V_2WS_4, and V_2WSe_4, respectively. These values are benchmarked against reported Na^+ ion diffusion barriers of representative 2D anode candidates such as BiC (0.217)[54], Si_3C (0.34 eV)[55], C_{18} (0.46)[56], Ti_3C_2 Mxene (0.09 eV)[57] VS_2 (0.085 eV)[58], h-BAs (0.248 eV)[59], B-doped g-CN/BC_3N_3 (0.73 eV)[60] CrSTe (0.32 eV)[61], Ti_2PS_2 (0.1 eV)[62], and TiS_2 (0.15 eV)[63]. In contrast, the energy barriers for K ions are consistently lower, at 0.162, 0.1612, 0.164, and 0.20 eV, respectively. Sodium generally exhibits a higher diffusion barrier compared to potassium. This difference is primarily due to potassium's larger atomic radius, which leads to weaker interactions with the host framework. Moreover, potassium ions are usually adsorbed farther from the host surface, reducing electrostatic adsorption and increasing ion mobility.

Charge transfer from the metal ion to the host is important because it stabilizes ion storage and improves anode performance. To elucidate the interaction mechanism between Na^+/K^+ ions and the host materials, the charge density difference ($\Delta\rho$) was calculated using the Equation (2) as shown below[64].

$$\Delta\rho = \rho_{V_2AB_4+Na/K} - \rho_{V_2AB_4} - \rho_{Na/K} \quad (2)$$

where $\rho_{V_2AB_4+Na/K}$ is the charge density of the system with the adsorbed Na^+ or K^+ ion, $\rho_{V_2AB_4}$ is the charge density of the pristine monolayer, and $\rho_{Na/K}$ is the charge density of the isolated ion. The charge density difference for Na^+ and K^+ adsorption on V_2AB_4 is shown in Figure 2D and Supplementary Figure 5. The $\Delta\rho$ maps reveal a large redistribution of charge upon the adsorption of alkali ions. Electron density depletion (cyan regions) is observed around the alkali-metal ions, whereas electron accumulation (yellow regions) occurs in the interstitial space between the ions and the surrounding chalcogen atoms. The amount of charge transfer was further quantified using Bader charge analysis; the charge transferred from the Na^+ and K^+ ions to four anode materials is approximately 0.82-0.84 e, respectively. This pronounced charge transfer reflects the cationic nature of the adsorbed alkali atoms and is beneficial for reversible ion storage. All four V_2AB_4 materials exhibit qualitatively similar charge-density difference patterns. The result suggests that these materials can accommodate different alkali ions via a common physicochemical mechanism, highlighting their promise as versatile hosts for alkali-ion anodes. To assess the impact of Na^+ and K^+ ion adsorption on the electronic properties, the projected density of states (PDOS) of single Na^+/K^+ ion-adsorbed V_2AB_4 systems was calculated, as shown in Figure 2E and Supplementary Figure 6. This behavior results from electron donation to the host lattice, causing the Fermi level (E_F) to shift into a region characterized by a higher density of transition-metal *d* states. The PDOS analysis reveals that the states in the vicinity of E_F show a predominant contribution from V 3d orbitals, along with further contributions from A-site d orbitals (Mo 4d or W 5d) and a small contribution from B-site chalcogen p orbitals (S 3p or Se 4p).

The electrochemical behavior of V_2AB_4 monolayers is schematically depicted in Figure 3A. In the figure above, reversible ion insertion and extraction at the anode and cathode, along with ion transport across the separator, are shown during the charge/discharge process. This schematic illustration provides a basic overview of the working principle of rechargeable batteries and a conceptual basis for evaluating the electrochemical performance of the proposed materials. Based on this framework, the electrochemical performance of electrode materials is evaluated by measuring their ion-storage capacity and open-circuit voltage (OCV). The studied layered topological material exhibits a high ion-storage capacity for Na^+ and K^+ ions, underscoring its potential for anodic energy storage applications. The ion-storage capability of V_2AB_4 (A = Mo or W, B = S or Se) monolayers is systematically evaluated by progressively increasing the concentration of Na^+ or K^+ ions in the host materials. The binding energies of Na^+ and K^+ ions decrease with increasing ion concentration, primarily due to repulsive interactions between adjacent ions. As depicted in Figure 3B, all systems exhibit negative binding energies over the entire adsorption range; thus, Na^+/K^+ uptake is thermodynamically favorable at high concentrations. The theoretical specific capacity was calculated according to the following Equation[65]:

$$C = \frac{nF}{3.6M} \quad (3)$$

where *n* is the number of adsorbed Na^+/K^+ atoms, *F* is Faraday's constant, and *M* is the molar mass of the pristine host material. Based on the maximum loading of Na^+ atoms, the Na^+ ion capacities are calculated to be 1,151 mAh g^{-1} for $V_8Mo_4S_{16}$, 730 mAh g^{-1} for $V_8Mo_4Se_{16}$, 907 mAh g^{-1} for $V_8W_4S_{16}$, and 624 mAh g^{-1} for $V_8W_4Se_{16}$. These values are substantially higher than that of hard carbon (~300 mAh g^{-1})[66] , the standard commercial sodium-ion anode, and are placed in comparison with computationally predicted 2D anodes evaluated under similar monolayer, full-surface-adsorption assumptions, including BiC (485 mAh g^{-1})[54], Si_3C (1,115 mAh g^{-1})[55], C_{18} (991.32 mAh g^{-1})[56], Ti_3C_2 Mxene (351.8 mAh g^{-1})[57], VS_2 (232 mAh g^{-1})[58], h-BAs (522 mAh g^{-1})[59], B-doped g-CN/BC_3N_3 (603.30 mAh g^{-1})[60] (CrSSe/CrSTe/CrSeTe: 260/198/177 mAh g^{-1})[61], Ti_2PS_2 (842 mAh g^{-1})[62], and TiS_2 (479 mAh g^{-1})[63]. We note that these capacities represent ideal upper bounds derived from full monolayer coverage; the practically accessible capacity is expected to be lower owing to

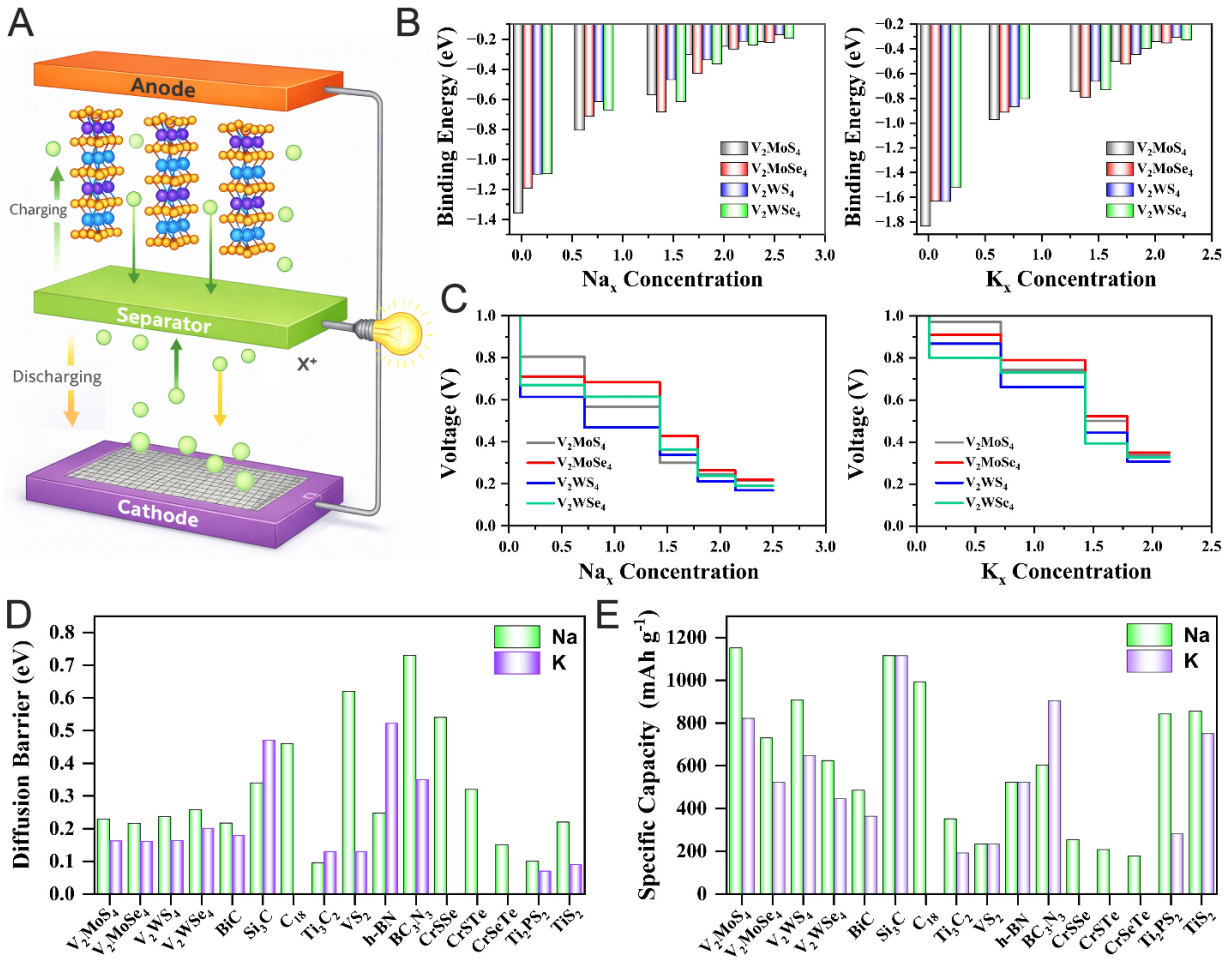

Figure 3. Sodium and potassium storage behavior and open-circuit voltage: (A) schematic of Na^+/K^+-ion transport during charge/discharge; (B) binding energies versus alkali concentration; (C) corresponding open-circuit voltage profiles; (D) comparison of Na^+/K^+ diffusion barriers; (E) comparison of theoretical specific capacities with representative anodes[54-63].

interlayer restacking, reduced electrochemically accessible surface area, irreversible adsorption at strong-binding sites, and electrode-level mass-loading constraints. The structural stability of fully sodiated and potassiated V_2AB_4 monolayers was further verified by AIMD simulations at maximum ion loading. The structures remained intact at high ion concentrations, without bond breaking or severe distortion, as shown in Supplementary Figure 7. Moreover, PDOS calculations for V_2AB_4 (A = Mo, W; B = S, Se) monolayers upon full Na^+/K^+ adsorption show a substantial increase in the density of states at the Fermi level, suggesting enhanced electrical conductivity [Supplementary Figure 8]. This is attributed to the strong charge transfer from Na^+/K^+ atoms to the substrate and the consequent contribution of alkali-metal states near the Fermi level, which increases the carrier density and promotes electronic conduction.

Another important parameter for battery operation is the OCV. The OCV during Na/K insertion is obtained using the following relation[67]:

$$V = -\frac{E_{Mx_2V_2AB_4} - E_{M_{x1}V_2AB_4} - (x_2 - x_1)\,E_M}{(x_2 - x_1)\,e} \tag{4}$$

where $E_{M_{x2}}V_2AB_4$, $E_{M_{x1}}V_2AB$ and EM are the total energies of $E_{M_{x2}}V_2AB_4$, $E_{M_{x1}}V_2AB_4$ and E_M is the energy per metal atom in the bulk respectively. As shown in Figure 3C, all V_2AB_4 monolayers exhibit a

step-like voltage profile with increasing Na/K ion concentration.

The OCV shows a similar decreasing trend as ion coverage increases, consistent with the variation observed in the binding energies. The Na^+ ion systems operate at lower voltages than their K-ion counterparts, which is generally favorable for anode applications, as it can lead to higher full-cell voltage and energy density. Overall, the combination of low diffusion barriers [Figure 3D] and high theoretical capacities [Figure 3E], relative to representative 2D anode materials, highlights the V_2AB_4 monolayers as promising anodes for next-generation Na^+ and K^+ ion batteries.

Interaction with electrolytes and salts

To further clarify the interfacial behavior of the V_2AB_4 monolayers in the Na^+/K^+ ion-anode environment, we analyzed their interactions with representative electrolyte species using adsorption-energy calculations.

Figure 4A schematically summarizes the electrolyte species considered and their modeled adsorption on the V_2AB_4 surfaces. The adsorption strength between electrolyte solvents/salts and the electrode surface provides useful information about molecular-level interfacial interactions. Accordingly, we evaluated the adsorption behavior of carbonate solvents and common Na^+/K^+ salts on the V_2AB_4 monolayers in the Na^+/K^+ ion-anode environment. The calculated adsorption energies are shown in Figure 4B. The adsorption energy values indicate favorable adsorption interactions between the electrolyte species and the V_2AB_4 surfaces, indicating strong molecular-level affinity in the optimized configurations. Figure 4C and Supplementary Figures 9-12 illustrate the optimized structural configurations of typical carbonate solvents, including diethyl carbonate (DEC), ethylene carbonate (EC), and fluoroethylene carbonate (FEC), and electrolyte salts, including sodium bis(fluorosulfonyl)imide (NaFSI), sodium hexafluorophosphate ($NaPF_6$), potassium bis(fluorosulfonyl)imide (KFSI), and potassium hexafluorophosphate (KPF_6), respectively, on V_2AB_4 (A = Mo/W, B = S/Se) monolayers. These adsorption-energy results describe the molecular-level interfacial interactions between V_2AB_4 and representative electrolyte species in Na^+/K^+ ion anode applications.

Sodium-polysulfide anchoring for sulfur cathode applications

In this section, we discuss electrochemical sodium-sulfur (Na-S) applications, particularly the reversible conversion of sulfur via sodium polysulfide species during charging and discharging. The reactions at the sulfur cathode are governed by ion transport, electron transfer, and phase conversion processes, which strongly influence reaction kinetics, cell-cycling stability, and sulfur utilization. In addition to anodic applications, the potential of V_2AB_4 monolayers as sulfur hosts is evaluated by examining the anchoring of sulfur and sodium polysulfide species, including elemental S_8, long-chain sodium polysulfides Na_2S_8, Na_2S_6, and Na_2S_4, and short-chain species Na_2S_2 and Na_2S. During discharge, these long-chain sodium polysulfides can dissolve in the liquid electrolyte, leading to the shuttle effect and capacity decay. A strong interaction between the host and polysulfides is necessary to immobilize these species and enable reversible reactions. For V_2AB_4 monolayers, adsorption energy data (see Figure 5A) indicate that all Na_2S_n species are strongly adsorbed on all four topological materials. Specifically, the adsorption energies of Na_2S_6 and Na_2S_8 exceed 1.5 eV, which is sufficient to prevent shuttling. The higher adsorption energies on S-based materials are attributed to the greater electronegativity of sulfur atoms, which results in stronger interactions with polysulfides. In contrast, Se-containing materials exhibit moderate adsorption energies that remain suitable for anchoring. However, excessively strong anchoring can cause a sluggish discharge process. Short-chain species demonstrate stronger chemical interactions, whereas long-chain species exhibit predominantly physical interactions. The adsorption configurations of Na_2S_n for all structures are shown in Supplementary Figures 13-16. The binding energies of these soluble species with common solvents, namely 1,2-dimethoxyethane (DME) and 1,3-dioxolane (DOL), were also calculated. The ether-based solvents (DME and DOL) considered here correspond specifically to the Na-S configuration, consistent with their standard

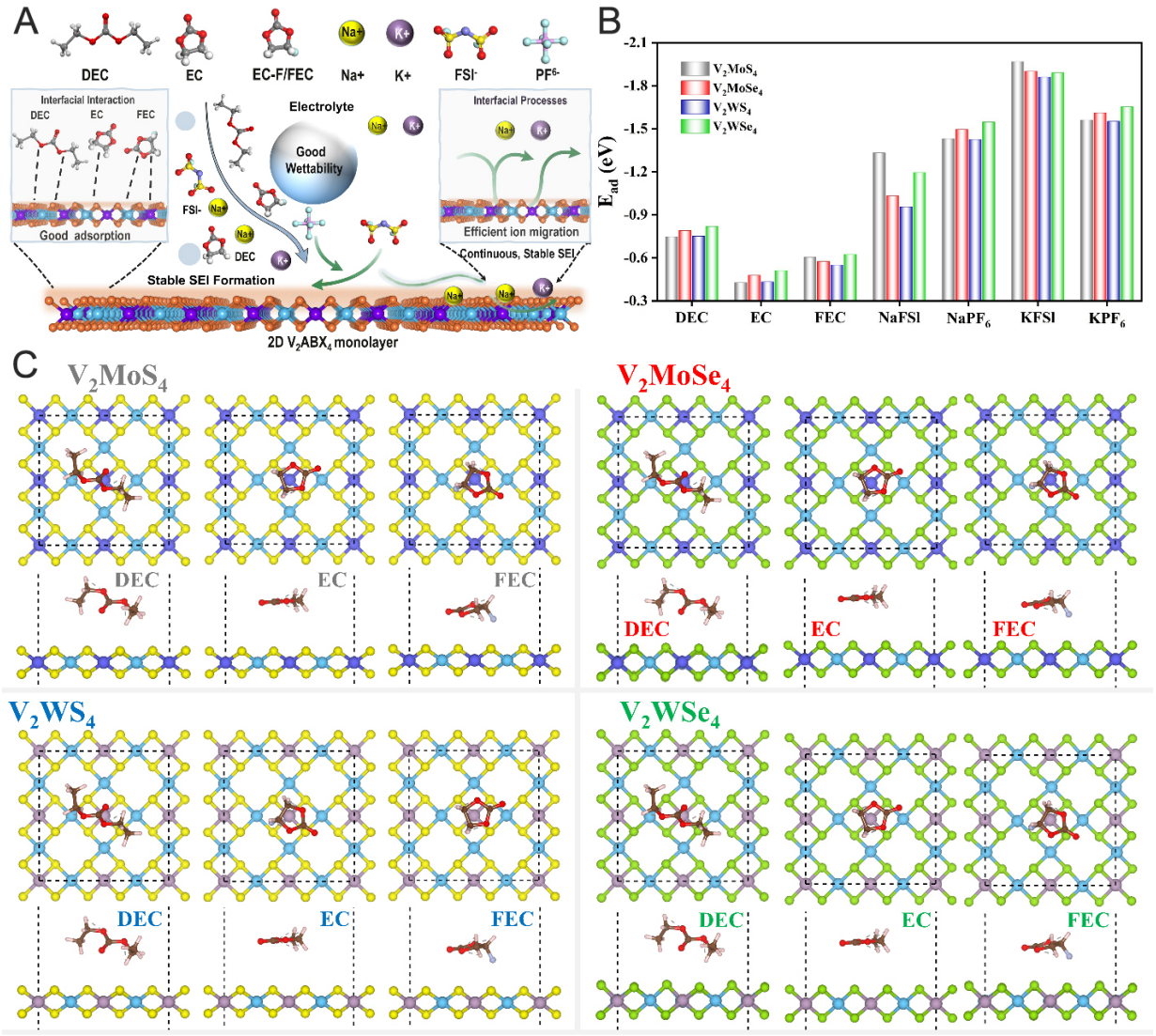

Figure 4. Electrolyte interaction with V_2AB_4 monolayers: (A) schematic representation of the interactions between representative electrolyte species and the V_2AB_4 surfaces; (B) corresponding adsorption energies of carbonate solvents and Na^+/K^+ salts on the V_2AB_4 substrates; (C) Top and side views of DEC, EC, and FEC adsorbed on V_2MoS_4, V_2MoSe_4, V_2WS_4, and V_2WSe_4 surfaces. DEC: Diethyl carbonate; EC: ethylene carbonate; FEC: fluoroethylene carbonate; NaFSI: sodium bis(fluorosulfonyl)imide; NaPF6: sodium hexafluorophosphate; KFSI: potassium bis(fluorosulfonyl)imide; KPF_6: potassium hexafluorophosphate.

use in Na-S chemistry. The interaction between soluble polysulfides and solvents is weaker than that with the V_2AB_4 monolayers. Collectively, the binding energies indicate strong binding and reversible conversion capability. The V_2AB_4 monolayers thus effectively immobilize sodium polysulfides, prevent their dissolution, and show significant promise as hosts for Na-S batteries.

The interaction mechanism between Na_2S_n clusters and V_2AB_4 monolayers was investigated using Bader charge analysis, as shown in Figure 5B. The results reveal a clear trend of increasing charge transfer with decreasing polysulfide chain length, ranging from approximately 0.15-0.33 e for long-chain Na_2S_8 and increasing to 0.84-0.91 e for the fully reduced Na_2S across the V_2AB_4 systems. This indicates progressively stronger chemical interactions between the V_2AB_4 substrates and short-chain species. To further elucidate this behavior, charge-density difference plots are presented in Figure 5C and Supplementary Figures 17-20. These plots demonstrate a distinct charge distribution at the interface after adsorption. Charge accumulation

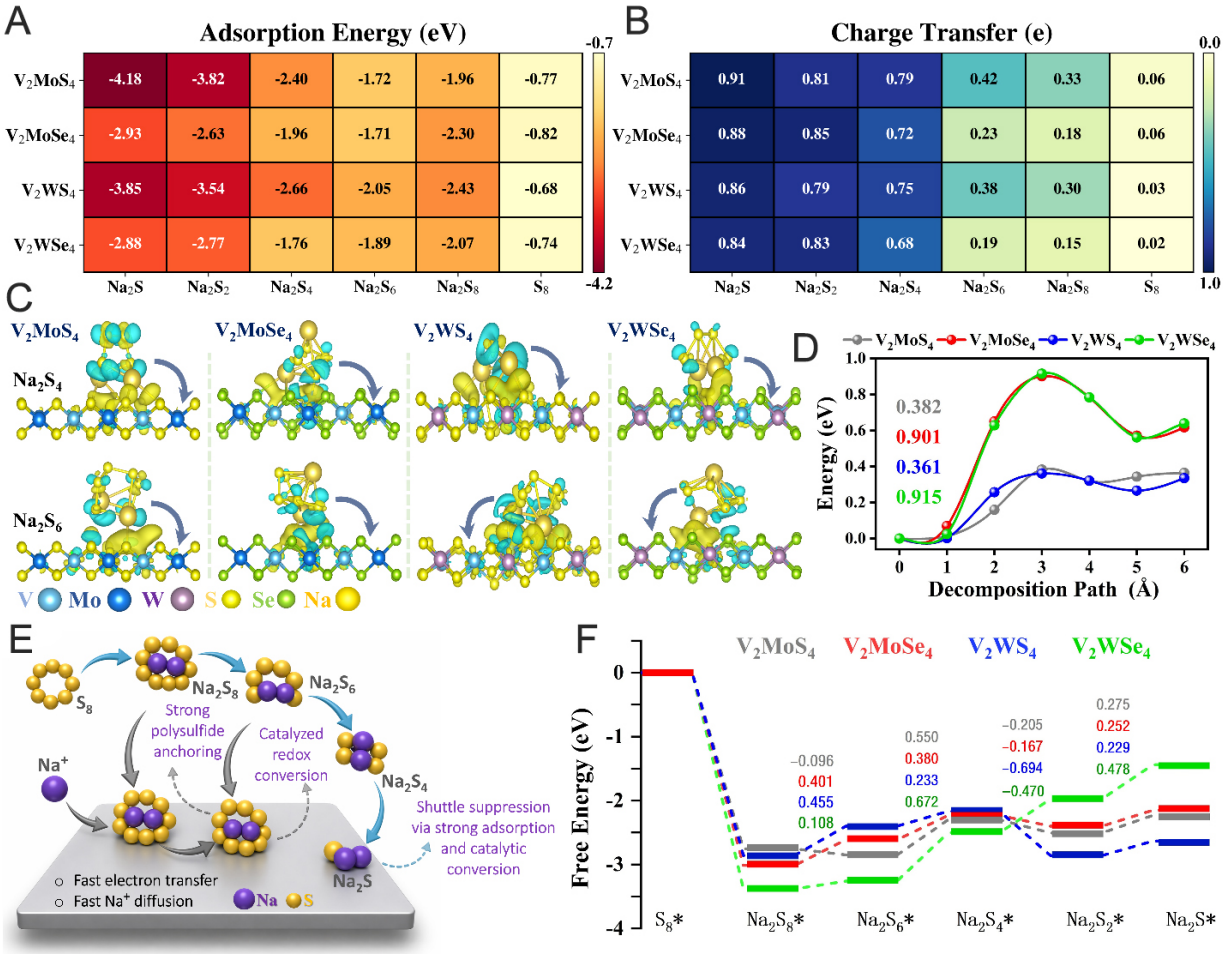

Figure 5. Insights into the sulfur cathode and anchoring role of V_2AB_4: (A) Adsorption energies of Na_2S_n clusters (n = 1, 2, 4, 6, and 8) and S_8; with the color scale representing the adsorption-energy values; (B) corresponding charge transfer to V_2MoS_4, V_2MoSe_4, V_2WS_4, and V_2WSe_4 hosts; with the color scale representing the transferred charge; (C) charge-density difference of intermediate-chain Na_2S_4 and long-chain Na_2S_6 polysulfides with all four topological materials. Yellow and cyan isosurfaces denote electron gain and electron loss, respectively. The atomic spheres represent V (light blue), Mo (dark blue), W (light purple), S (small yellow), Se (green), and Na (large yellow); (D) Decomposition energy barriers of Na_2S adsorbed on the V_2AB_4 monolayers; (E) Schematic illustration of the catalytic mechanism, highlighting strong polysulfide anchoring, accelerated redox conversion, suppressed shuttle effect, and rapid electron transport. In panel (E), purple and golden-yellow spheres represent Na and S, respectively; (F) Gibbs free-energy profiles for the S_8 to Na_2S sulfur reduction reaction on all monolayers.

occurs primarily at the surface atoms of V_2AB_4, while charge depletion is concentrated within the Na_2S_n clusters, indicating electron transfer from the sodium polysulfides to the substrates. This charge redistribution is considerably more pronounced for short-chain species than for long-chain species. Overall, the charge-density difference and Bader charge analyses confirm that V_2AB_4 monolayers exhibit physicochemical interactions with sodium polysulfide intermediates, which are essential for suppressing the shuttle effect and improving the cycling stability of Na-S batteries. To further investigate the electronic properties of Na_2S_n species adsorbed on the V_2AB_4 substrates, the PDOS was calculated and analyzed, as presented in Supplementary Figures 21-24. The electronic states near the Fermi level are dominated by V-3d and Mo/W-d orbitals, with contributions from S/Se-p states, indicating interfacial coupling and charge redistribution upon adsorption. Across all configurations, the continuous states around the Fermi level confirm the metallic character of the adsorbed system. Overall, these results confirm effective electronic coupling between the host material and the Na_2S_n species, which facilitates redox reactions in Na-S batteries.

Next, the catalytic decomposition barrier of the discharge product Na_2S is calculated using the CI-NEB method[52,68]. During charging of Na-S batteries, the final insoluble product, Na_2S, exhibits low electronic conductivity and a high decomposition energy barrier, thereby increasing overpotential and slowing the reaction rate. The electrochemical performance of the Na-S battery system is governed by the decomposition kinetics of sodium sulfide (Na_2S), which involve cleavage of Na-S bonds and migration of Na^+ ions across the surface. The decomposition reaction, $*Na_2S \rightarrow *NaS + Na^+ + e^-$, proceeds through cleavage of a Na-S bond at the adsorption site, followed by migration of the released Na^+ ion to a neighboring site. The decomposition energy barriers for Na_2S adsorbed on the V_2AB_4 monolayers are shown in Figure 5D. The calculated decomposition energy barriers are 0.382, 0.901, 0.361, and 0.915 eV for V_2MoS_4, V_2MoSe_4, V_2WS_4, and V_2WSe_4, respectively. These values are significantly lower than the decomposition barrier for isolated Na_2S in the gas phase and are comparable to, or lower than, those of many previously reported Na-S host materials, including Cr@NG (1.54 eV)[69], Fe@NG (1.16 eV)[69], COP (0.68 eV)[70] Co@NG (1.17 eV)[69], V@WSe_2 (0.99 eV)[71], Fe@MoS_2 (1.08 eV)[72], Ni@MoS_2 (1.34 eV)[71], $HfTiTe_4$ (0.917)[16], $ZrTiTe_4$ (0.89)[16], $HfZrTe_4$ (0.83)[16], $Mo_2TiC_2S_2$ (1.59 eV)[73], $Mo_2TiC_2O_2$ (1.67 eV)[73], MnN_4/C (1.52 eV), and YN_4/C (1.52 eV)[74]. The lowered energy barriers suggest that the V_2AB_4-type surfaces can activate the oxidative decomposition of Na_2S during charging. Figure 5E schematically illustrates that V_2AB_4 monolayers serve as effective hosts for Na-S cathodes by strongly anchoring sodium polysulfides and promoting their catalytic redox conversion. During cycling, these monolayers suppress the polysulfide shuttle effect through robust adsorption and surface catalysis. In addition, enhanced electron transfer and rapid Na^+ diffusion kinetics improve reaction efficiency, sulfur utilization, and the overall electrochemical performance of Na-S batteries. Finally, the conversion of sulfur on V_2MoSe_4, V_2MoS_4, V_2WS_4, and V_2WSe_4 monolayers involves multiple reaction steps, starting from sulfur crown (S_8) and ultimately reducing to the short-chain sulfide Na_2S. The overall sulfur reduction reaction during the discharge process of Na-S batteries can be described as a 16-electron conversion[53]:

$$S_8 + 16Na^+ + 16e^- \rightarrow 8Na_2S \tag{5}$$

The SRR with elementary steps is given below (* denotes the adsorbed species):

$$*S_8 + 2Na^+ + 2e^- \rightarrow *Na_2S_8 \tag{6}$$

$$*Na_2S_8 \rightarrow *Na_2S_6 + 1/4S_8 \tag{7}$$

$$*Na_2S_6 \rightarrow *Na_2S_4 + 1/4S_8 \tag{8}$$

$$*Na_2S_4 \rightarrow *Na_2S_2 + 1/4S_8 \tag{9}$$

$$*Na_2S_2 \rightarrow *Na_2S + 1/8S_8 \tag{10}$$

The Gibbs free-energy change of each elementary step was calculated using Equation (1), and the resulting profiles are presented in Figure 5F. Initially, the discharge process converts S_8 into a series of soluble sodium polysulfides, including Na_2S_8, Na_2S_6, and Na_2S_4, which are subsequently reduced to short-chain molecules (Na_2S_2) and ultimately to the insoluble product Na_2S. The Gibbs free-energy profile for the conversion of S_8 to Na_2S on V_2AB_4 monolayers provides insight into the reaction mechanism and catalytic properties. The reduction of S_8 to Na_2S_8 is highly exergonic for all materials, indicating that adsorption and activation of sulfur species occur spontaneously. The reaction step with the largest positive Gibbs free-energy change (ΔG) is considered the rate-limiting step of the sulfur reduction reaction. The calculated maximum Gibbs free-energy changes (ΔG) for V_2MoSe_4, V_2MoS_4, V_2WS_4, and V_2WSe_4 are 0.401, 0.55, 0.450, and 0.672 eV, respectively. These findings show that all V_2AB_4 monolayers possess comparable thermodynamic favorability

for sulfur reduction. The catalytic performance is further evaluated by comparing it with a wide range of previously reported Na-S electrocatalysts. The rate-limiting step for sulfur reduction on V_2MoSe_4 (0.401 eV) is substantially lower than those of Co-V@N-C (1.11 eV)[75], Cr-V@N-C (2.09 eV)[75], AP-C[76] (0.88), ZP-C (0.80)[76], AZP-C (0.75)[76], Cr-Cr@N-C (2.09 eV)[75], and V-V@N-C (2.14 eV)[75], and is also lower than Fe-Co/NC (0.65 eV)[77], Co/NC (0.70 eV)[77], and Fe/NC (0.73 eV)[77]. Additionally, it outperforms transition-metal carbide systems such as $Mo_2TiC_2S_2$ (0.85 eV)[73], $Mo_2TiC_2O_2$ (1.24 eV)[73], and Mo_2C (0.92 eV)[78]. These findings demonstrate that V_2AB_4 monolayers possess highly competitive catalytic activity for both sulfur reduction and Na_2S decomposition, positioning them among the most efficient Na-S electrocatalysts.

CONCLUSION

This research highlights that the 2D topological monolayers V_2MoS_4, V_2MoSe_4, V_2WS_4, and V_2WSe_4 perform well in two distinct cell configurations as high-capacity sodium anodes and as catalytically efficient hosts for the Na-S cathode. These materials, particularly V_2MoS_4, exhibit a high theoretical capacity of ≈1,151 mAh g^{-1}, a low diffusion barrier of ≈0.229 eV, and a moderate open-circuit voltage of 0.21 V for sodium-ion anodes. Collectively, these metrics suggest that these materials are more competitive than conventional graphitic carbon electrodes. Benefiting from their topological electronic character, these surfaces provide strong anchoring for sodium polysulfides, thereby constraining the dissolution of long-chain sodium polysulfides in the liquid electrolyte (DME/DOL), suppressing the shuttle effect, and rendering the catalytic reactions for sulfur reduction energetically feasible. The calculated Gibbs free-energy changes (ΔG_{max}) range from 0.401 eV to 0.672 eV, while Na_2S decomposition barriers range from 0.361 eV to 0.915 eV, confirming favorable thermodynamic and kinetic characteristics across all systems. The intact geometric structures of these materials at room temperature, together with their dynamic stability, provide a favorable environment for Na^+ ion intercalation and sulfur reduction. This atomic-level study highlights the potential of these 2D topological vanadium chalcogenide materials as versatile electrode materials that combine high-capacity alkali-ion storage with efficient polysulfide conversion across two distinct cell configurations.

DECLARATIONS

Authors' contributions

Conceptualization, methodology, investigation, formal analysis, data curation, visualization, writing - original draft, funding acquisition, supervision, project administration: Ghani, A.
Formal analysis, data curation, writing - review & editing: Ahmed, S.
Investigation, writing - review & editing: Bilal, M.
Validation, writing - review & editing: Murtaza, A.
Validation, resources, writing - review & editing: Du, H.
Methodology, validation, writing - review & editing: Muhammad, I.

Availability of data and materials

The data supporting the findings of this study are available within the article and its Supplementary Materials. Additional information can be obtained from the corresponding authors upon reasonable request.

AI and AI-assisted tools statement

Not applicable.

Financial support and sponsorship

The authors acknowledge the support from the Initiation Funds for High-level Talents Program of Xi'an International University (Grant No. XAIU2025116), the National Natural Science Foundation of China, including the Research Fund for International Young Scientists (RFIS-I, Grant No. W2433117), as well as the Ministry of Science and Technology of China (QN2022170004L).

Conflicts of interest

All authors declared that there are no conflicts of interest.

Ethical approval and consent to participate

Not applicable.

Consent for publication

Not applicable.

Supplementary Materials

Supplementary Materials

REFERENCES

1. Wu, Y.; Shuang, W.; Wang, Y.; et al. Recent progress in sodium-ion batteries: advanced materials, reaction mechanisms and energy applications. *Electrochem. Energy. Rev.* **2024**, *7*, 215. DOI
2. Hirsh, H. S.; Li, Y.; Tan, D. H. S.; et al. Sodium-ion batteries paving the way for grid energy storage. *Adv. Energy. Mater.* **2020**, *10*, 2001274. DOI
3. Chayambuka, K.; Mulder, G.; Danilov, D. L.; Notten, P. H. L. Sodium-ion battery materials and electrochemical properties reviewed. *Adv. Energy. Mater.* **2018**, *8*, 1800079. DOI
4. Zhang, H.; Wang, L.; Zuo, P. Advances in sodium-ion battery cathode materials: exploring chemistry, reaction mechanisms, and prospects for next-generation energy storage systems. *J. Mater. Chem. A.* **2024**, *12*, 30971-1003. DOI
5. Peng, B.; Zhou, Z.; Shi, J.; Huang, X.; Li, Y.; Ma, L. Earth-abundant Fe-Mn-based compound cathodes for sodium-ion batteries: challenges and progress. *Adv. Funct. Mater.* **2024**, *34*, 2311816. DOI
6. Huang, H.; Wu, X.; Gao, Y.; et al. Polyanionic cathode materials: a comparison between Na-ion and K-ion batteries. *Adv. Energy. Mater.* **2024**, *14*, 2304251. DOI
7. Zhang, H.; Gao, Y.; Liu, X.; et al. Long-cycle-life cathode materials for sodium-ion batteries toward large-scale energy storage systems. *Adv. Energy. Mater.* **2023**, *13*, 2300149. DOI
8. He, X.; Iqbal, N.; Ghani, U.; Li, T. Potassium ion batteries: recent advancements in anodic, cathodic, and electrolytic materials. *J. Alloys. Compd.* **2024**, *981*, 173680. DOI
9. Ma, M.; Chong, S.; Yao, K.; Liu, H. K.; Dou, S. X.; Huang, W. Advanced anode materials for potassium batteries: sorting out opportunities and challenges by potassium storage mechanisms. *Matter* **2023**, *6*, 3220-73. DOI
10. Luo, G.; Feng, X.; Qian, M.; et al. State-of-art progress and perspectives on alloy-type anode materials for potassium-ion batteries. *Mater. Chem. Front.* **2023**, *7*, 3011-36. DOI
11. Lei, Y. J.; Lu, X.; Yoshikawa, H.; et al. Understanding the charge transfer effects of single atoms for boosting the performance of Na-S batteries. *Nat. Commun.* **2024**, *15*, 3325. DOI PubMed PMC
12. He, J.; Bhargav, A.; Su, L.; Charalambous, H.; Manthiram, A. Intercalation-type catalyst for non-aqueous room temperature sodium-sulfur batteries. *Nat. Commun.* **2023**, *14*, 6568. DOI PubMed PMC
13. Lin, Z.; Liu, Z.; Fu, W.; Dudney, N. J.; Liang, C. Lithium polysulfidophosphates: a family of lithium-conducting sulfur-rich compounds for lithium-sulfur batteries. *Angew. Chem. Int. Ed.* **2013**, *52*, 7460-3. DOI
14. Fan, F. Y.; Pan, M. S.; Lau, K. C.; et al. Solvent effects on polysulfide redox kinetics and ionic conductivity in lithium-sulfur batteries. *J. Electrochem. Soc.* **2016**, *163*, A3111-6. DOI
15. Wang, Y.; Guo, T.; Alhajji, E.; et al. MXenes for sulfur-based batteries. *Adv. Energy. Mater.* **2023**, *13*, 2202860. DOI
16. Ahmed, S.; Ghani, A.; Mehmood, R.; et al. Ultra-stable topological telluride monolayers for next-generation battery anodes and sulfur hosts. *Adv. Sci.* **2026**, *13*, e15841. DOI
17. Muhammad, I.; Ahmed, S.; Yao, Z.; Khan, D.; Hussain, T.; Wang, Y. G. First-row transition metal carbide nanosheets as high-performance cathode materials for lithium-sulfur batteries. *Nanoscale* **2023**, *16*, 262-72. DOI
18. Chen, X.; Peng, H.; Zhang, R.; et al. An analogous periodic law for strong anchoring of polysulfides on polar hosts in lithium sulfur batteries: S- or Li-binding on first-row transition-metal sulfides? *ACS. Energy. Lett.* **2017**, *2*, 795-801. DOI
19. Chen, Z.; Lv, W.; Kang, F.; Li, J. Theoretical investigation of the electrochemical performance of transition metal nitrides for lithium-sulfur batteries. *J. Phys. Chem. C.* **2019**, *123*, 25025-30. DOI

20. Yang, W.; Chen, D.; She, Y.; et al. Rational design of vanadium chalcogenides for sodium-ion batteries. *J. Power. Sources.* **2020**, *478*, 228769. DOI
21. Xu, Y.; Ma, H.; Zhong, A.; et al. Unveiling the confined space charge storage mechanism in vanadium chalcogenides/carbon mixed conductor interface for potassium-ion batteries. *Small. Methods.* **2025**, *9*, e2500541. DOI
22. Hossain, M.; Zhang, H.; Huangfu, Y.; et al. 2D metallic vanadium dichalcogenides and related heterostructures. *Mater. Today. Adv.* **2024**, *21*, 100451. DOI
23. Liu, D.; Xie, S.; Zhan, Z.; et al. High crystalline VSe_2@PANI collaborating with ether electrolyte to construct efficient sodium-ion storage interface. *Chem. Eng. J.* **2025**, *524*, 169039. DOI
24. Ming, F.; Liang, H.; Lei, Y.; Zhang, W.; Alshareef, H. N. Solution synthesis of VSe_2 nanosheets and their alkali metal ion storage performance. *Nano. Energy.* **2018**, *53*, 11-6. DOI
25. Xia, W.; Liu, H.; Chen, Y.; et al. Linking D-band center modulation with rapid reversible sulfur conversion kinetics via structural engineering of VS_2. *Small* **2025**, *21*, e2408304. DOI
26. Huang, T.; Cheng, K.; Lin, C.; Fu, Y.; Lin, S.; Chen, Y. Two-dimensional metallic VTe_2 demonstrating fast ion diffusion for aqueous zinc-ion batteries. *Sustain. Energy. Fuels.* **2022**, *6*, 4626-35. DOI
27. Yang, C.; Ou, X.; Xiong, X.; et al. V_5S_8-graphite hybrid nanosheets as a high rate-capacity and stable anode material for sodium-ion batteries. *Energy. Environ. Sci.* **2017**, *10*, 107-13. DOI
28. Syed, W. A.; Kakarla, A. K.; Bandi, H.; Shanthappa, R.; Yu, J. S. Improved rate and cycling capability of V_2O_5@MoS_2 nanocomposites as an advanced cathode material for rechargeable aqueous zinc-ion batteries. *Sustain. Mater. Technol.* **2024**, *40*, e00968. DOI
29. Ortiz, B. R.; Gomes, L. C.; Morey, J. R.; et al. New kagome prototype materials: discovery of KV_3Sb_5,RbV_3Sb_5, and CsV_3Sb_5. *Phys. Rev. Mater.* **2019**, *3*, 094407. DOI
30. Ortiz, B. R.; Teicher, S. M. L.; Hu, Y.; et al. CsV_3Sb_5: A Z_2 topological kagome metal with a superconducting ground state. *Phys. Rev. Lett.* **2020**, *125*, 247002. DOI
31. Cho, S.; Ma, H.; Xia, W.; et al. Emergence of new van hove singularities in the charge density wave state of a topological kagome metal RbV_3Sb_5. *Phys. Rev. Lett.* **2021**, *127*, 236401. DOI
32. Pokharel, G.; Teicher, S. M. L.; Ortiz, B. R.; et al. Electronic properties of the topological kagome metals YV_6Sn_6 and GdV_6Sn_6. *Phys. Rev. B.* **2021**, *104*, 235139. DOI
33. Hu, Y.; Ma, J.; Li, Y.; et al. Phonon promoted charge density wave in topological kagome metal ScV_6Sn_6. *Nat. Commun.* **2024**, *15*, 1658. DOI
34. Zhang, Y.; Zhang, X.; Liu, G.; et al. Accelerating sulfur conversion kinetics by topological semimetal electrocatalysts Pd_3Sn for high-performance Li-S batteries. *Adv. Funct. Mater.* **2025**, *35*, 2417750. DOI
35. Jiang, Y.; Wang, H.; Bao, K.; Liu, Z.; Wang, J. Monolayer V_2MX_4: a new family of quantum anomalous hall insulators. *Phys. Rev. Lett.* **2024**, *132*, 106602. DOI
36. Crossland, C. J.; Hickey, P. J.; Evans, J. S. O. The synthesis and characterisation of Cu_2MX_4 (M = W or Mo; X = S, Se or S/Se) materials prepared by a solvothermal method. *J. Mater. Chem.* **2005**, *15*, 3452. DOI
37. Chen, W.; Chen, H.; Zhu, H.; et al. Solvothermal synthesis of ternary Cu_2MoS_4 nanosheets: structural characterization at the atomic level. *Small* **2014**, *10*, 4637-44. DOI
38. Tan, C.; Yu, P.; Hu, Y.; et al. High-yield exfoliation of ultrathin two-dimensional ternary chalcogenide nanosheets for highly sensitive and selective fluorescence DNA sensors. *J. Am. Chem. Soc.* **2015**, *137*, 10430-6. DOI
39. Bainsla, L.; Zhao, B.; Behera, N.; et al. Large out-of-plane spin-orbit torque in topological Weyl semimetal $TaIrTe_4$. *Nat. Commun.* **2024**, *15*, 4649. DOI
40. Liu, Z. L.; Wu, X.; Shao, Y.; et al. Epitaxially grown monolayer VSe_2: an air-stable magnetic two-dimensional material with low work function at edges. *Sci. Bull.* **2018**, *63*, 419-25. DOI
41. van Efferen, C.; Berges, J.; Hall, J.; et al. A full gap above the Fermi level: the charge density wave of monolayer VS_2. *Nat. Commun.* **2021**, *12*, 6837. DOI PubMed PMC
42. Kresse, G.; Furthmüller, J. Efficient iterative schemes for ab initio total-energy calculations using a plane-wave basis set. *Phys. Rev. B.* **1996**, *54*, 11169. DOI PubMed
43. Kresse, G.; Joubert, D. From ultrasoft pseudopotentials to the projector augmented-wave method. *Phys. Rev. B.* **1999**, *59*, 1758-75. DOI
44. Perdew, J. P.; Burke, K.; Ernzerhof, M. Generalized gradient approximation made simple. *Phys. Rev. Lett.* **1996**, *77*, 3865-8. DOI PubMed
45. Grimme, S.; Antony, J.; Ehrlich, S.; Krieg, H. A consistent and accurate ab initio parametrization of density functional dispersion correction (DFT-D) for the 94 elements H-Pu. *J. Chem. Phys.* **2010**, *132*, 154104. DOI PubMed

46. Grimme, S.; Ehrlich, S.; Goerigk, L. Effect of the damping function in dispersion corrected density functional theory. *J. Comput. Chem.* **2011**, *32*, 1456-65. DOI PubMed
47. Dudarev, S. L.; Botton, G. A.; Savrasov, S. Y.; Humphreys, C. J.; Sutton, A. P. Electron-energy-loss spectra and the structural stability of nickel oxide: an LSDA+U study. *Phys. Rev. B.* **1998**, *57*, 1505-9. DOI
48. Togo, A.; Tanaka, I. First principles phonon calculations in materials science. *Scr. Mater.* **2015**, *108*, 1-5. DOI
49. Togo, A.; Chaput, L.; Tanaka, I. Distributions of phonon lifetimes in Brillouin zones. *Phys. Rev. B.* **2015**, 91. DOI
50. Nosé, S. A unified formulation of the constant temperature molecular dynamics methods. *J. Chem. Phys.* **1984**, *81*, 511-9. DOI
51. Hoover, W. G. Canonical dynamics: equilibrium phase-space distributions. *Phys. Rev. A. Gen. Phys.* **1985**, *31*, 1695-7. DOI PubMed
52. Henkelman, G.; Uberuaga, B. P.; Jónsson, H. A climbing image nudged elastic band method for finding saddle points and minimum energy paths. *J. Chem. Phys.* **2000**, *113*, 9901-4. DOI
53. Jayan, R.; Islam, M. M. Mechanistic insights into interactions of polysulfides at VS_2 interfaces in Na-S batteries: a DFT study. *ACS. Appl. Mater. Interfaces.* **2021**, *13*, 35848-55. DOI PubMed
54. Ghani, A.; Ahmed, S.; Murtaza, A.; et al. Bi-C monolayer as a promising 2D anode material for Li, Na, and K-ion batteries. *Phys. Chem. Chem. Phys.* **2023**, *25*, 4980-6. DOI
55. Wang, Y.; Li, Y. *Ab initio* prediction of two-dimensional Si_3C enabling high specific capacity as an anode material for Li/Na/K-ion batteries. *J. Mater. Chem. A.* **2020**, *8*, 4274-82. DOI
56. Younis, U.; Muhammad, I.; Kawazoe, Y.; Sun, Q. Design of tetracene-based metallic 2D carbon materials for Na- and K-Ion batteries. *Appl. Surf. Sci.* **2020**, *521*, 146456. DOI
57. Er, D.; Li, J.; Naguib, M.; Gogotsi, Y.; Shenoy, V. B. Ti_3C_2 MXene as a high capacity electrode material for metal (Li, Na, K, Ca) ion batteries. *ACS. Appl. Mater. Interfaces.* **2014**, *6*, 11173-9. DOI
58. Putungan, D. B.; Lin, S. H.; Kuo, J. L. Metallic VS_2 monolayer polytypes as potential sodium-ion battery anode via ab initio random structure searching. *ACS. Appl. Mater. Interfaces.* **2016**, *8*, 18754-62. DOI PubMed
59. Khossossi, N.; Banerjee, A.; Benhouria, Y.; Essaoudi, I.; Ainane, A.; Ahuja, R. Ab initio study of a 2D h-BAs monolayer: a promising anode material for alkali-metal ion batteries. *Phys. Chem. Chem. Phys.* **2019**, *21*, 18328-37. DOI PubMed
60. Xia, X.; Yin, H.; Zhang, Y.; Huang, S. Boron-doped g-CN monolayer as a promising anode for Na/K-ion batteries. *Surf. Interfaces.* **2023**, *36*, 102479. DOI
61. Sahoo, S.; Kumari, P.; Ray, S. J. CrXY (X/Y = S, Se, Te) monolayers as efficient anode materials for Li and Na-ion batteries: a first-principles study. *RSC. Adv.* **2024**, *14*, 5771-81. DOI PubMed PMC
62. Ge, B.; Chen, B.; Li, L. Ternary transition metal chalcogenides Ti_2PX_2 (X = S, Se, Te) anodes for high performance metal-ion batteries: a DFT study. *Appl. Surf. Sci.* **2021**, *550*, 149177. DOI
63. Samad, A.; Shafique, A.; Shin, Y. H. Adsorption and diffusion of mono, di, and trivalent ions on two-dimensional TiS_2. *Nanotechnology* **2017**, *28*, 175401. DOI PubMed
64. Khossossi, N.; Singh, D.; Banerjee, A.; et al. High-specific-capacity and high-performing post-lithium-ion battery anode over 2D black arsenic phosphorus. *ACS. Appl. Energy. Mater.* **2021**, *4*, 7900-10. DOI
65. Shukla, V.; Araujo, R. B.; Jena, N. K.; Ahuja, R. The curious case of two dimensional Si_2BN: a high-capacity battery anode material. *Nano. Energy.* **2017**, *41*, 251-60. DOI
66. Stevens, D. A.; Dahn, J. R. High capacity anode materials for rechargeable sodium-ion batteries. *J. Electrochem. Soc.* **2000**, *147*, 1271-3. DOI
67. Xiang, P.; Sharma, S.; Wang, Z. M.; Wu, J.; Schwingenschlögl, U. Flexible C_6BN monolayers as promising anode materials for high-performance K-ion batteries. *ACS. Appl. Mater. Interfaces.* **2020**, *12*, 30731-9. DOI PubMed PMC
68. Henkelman, G.; Jónsson, H. Improved tangent estimate in the nudged elastic band method for finding minimum energy paths and saddle points. *J. Chem. Phys.* **2000**, *113*, 9978-85. DOI
69. Jayan, R.; Islam, M. M. Single-atom catalysts for improved cathode performance in Na-S batteries: a density functional theory (DFT) study. *J. Phys. Chem. C.* **2021**, *125*, 4458-67. DOI
70. Wang, L.; Wang, S.; Wu, L.; et al. CoP as a bidirectional catalyst: unlocking reaction dynamics in sodium-sulfur batteries. *J. Power. Sources.* **2025**, *655*, 238004. DOI
71. Cao, B.; Liu, H.; Zhang, P.; et al. Flexible MXene framework as a fast electron/potassium-ion dual-function conductor boosting stable potassium storage in graphite electrodes. *Adv. Funct. Mater.* **2021**, *31*, 2102126. DOI
72. Jayan, R.; Islam, M. M. Design principles of bifunctional electrocatalysts for engineered interfaces in Na-S batteries. *ACS. Catal.* **2021**, *11*, 15149-61. DOI

73. Nahian, M. S.; Jayan, R.; Kaewmaraya, T.; Hussain, T.; Islam, M. M. Elucidating synergistic mechanisms of adsorption and electrocatalysis of polysulfides on double-transition metal MXenes for Na-S batteries. *ACS. Appl. Mater. Interfaces.* **2022**, *14*, 10298-307. DOI PubMed
74. Zhang, E.; Hu, X.; Meng, L.; et al. Single-atom yttrium engineering janus electrode for rechargeable Na-S batteries. *J. Am. Chem. Soc.* **2022**, *144*, 18995-9007. DOI
75. Fan, K.; Ying, Y.; Lin, Z.; Tsang, Y. H.; Huang, H. Building up an "elemental property-adsorption energy descriptor-decomposition barrier" three-tier model for screening biatom catalysts in sodium-sulfur batteries. *Adv. Energy. Mater.* **2023**, *13*, 2300871. DOI
76. Wang, L.; Luo, X.; Cao, X.; et al. Dual pentagonal defects in metal-free carbon enable synergistic catalysis for sodium-sulfur batteries. *J. Power. Sources.* **2026**, *668*, 239376. DOI
77. Li, C.; Yu, J.; Yang, D.; et al. Balancing electronic spin state via atomically-dispersed heteronuclear Fe-Co pairs for high-performance sodium-sulfur batteries. *J. Am. Chem. Soc.* **2025**, *147*, 8250-9. DOI
78. Zhou, X.; Yu, Z.; Yao, Y.; et al. A high-efficiency Mo_2C electrocatalyst promoting the polysulfide redox kinetics for Na-S batteries. *Adv. Mater.* **2022**, *34*, e2200479. DOI